



# The Magnetic Field of the Active Planet-hosting M Dwarf AU Mic

Oleg Kochukhov<sup>1</sup> and Ansgar Reiners<sup>2</sup> <sup>1</sup> Department of Physics and Astronomy, Uppsala University, Box 516, SE-75120 Uppsala, Sweden; [oleg.kochukhov@physics.uu.se](mailto:oleg.kochukhov@physics.uu.se)<sup>2</sup> Institut für Astrophysik, Georg-August-Universität, Friedrich-Hund-Platz 1, D-37077 Göttingen, Germany

Received 2020 August 4; revised 2020 August 24; accepted 2020 August 24; published 2020 October 9

## Abstract

AU Mic is a young, very active M dwarf star with a debris disk and at least one transiting Neptune-size planet. Here we present a detailed analysis of the magnetic field of AU Mic based on previously unpublished high-resolution optical and near-infrared spectropolarimetric observations. We report a systematic detection of circular and linear polarization signatures in the stellar photospheric lines. Tentative Zeeman Doppler imaging modeling of the former data suggests a nonaxisymmetric global field with a surface-averaged strength of about 90 G. At the same time, linear polarization observations indicate the presence of a much stronger  $\approx 2$  kG axisymmetric dipolar field, which contributes no circular polarization signal due to the equator-on orientation of AU Mic. A separate Zeeman broadening and intensification analysis allowed us to determine a mean field modulus of 2.3 and 2.1 kG from the *Y*- and *K*-band atomic lines, respectively. These magnetic field measurements are essential for understanding environmental conditions within the AU Mic planetary system.

*Unified Astronomy Thesaurus concepts:* [Stellar activity \(1580\)](#); [Stellar magnetic fields \(1610\)](#); [M dwarf stars \(982\)](#)

## 1. Introduction

Magnetism plays a prominent role in the physics of low-mass stars and their planetary systems. M dwarfs are known to exhibit copious evidence of magnetically driven surface activity in the form of flares, photometric rotational modulation, and chromospheric and coronal emission (e.g., Hawley et al. 2014; Newton et al. 2016, 2017; Astudillo-Defru et al. 2017; Wright et al. 2018). Direct magnetic field measurements demonstrate that these objects possess some of the strongest fields found in cool active stars (Morin et al. 2008; Kochukhov & Lavail 2017; Shulyak et al. 2017). M-dwarf surface magnetic field geometries have a complex, multicomponent nature (Reiners & Basri 2009; Afram & Berdyugina 2019; Kochukhov & Shulyak 2019) with a moderately strong, often axisymmetric, global field component measured with high-resolution circular polarimetry (Donati et al. 2006, 2008b; Morin et al. 2008, 2010; Lavail et al. 2018) superimposed onto a much stronger tangled small-scale field that gives rise to Zeeman broadening and splitting in the intensity spectra (Saar & Linsky 1985; Johns-Krull & Valenti 1996; Reiners & Basri 2006; Kochukhov et al. 2009; Shulyak et al. 2017, 2019). The relationship between these two magnetic components is currently poorly characterized as a function of stellar rotation and fundamental parameters and is not reproduced by theoretical models of dynamo operating in fully convective stars (Dobler et al. 2006; Browning 2008; Yadav et al. 2015).

M-dwarf magnetism has dramatic consequences for the close-in terrestrial planets orbiting these stars. Global magnetic fields of low-mass stars modulate their X-ray activity (Cook et al. 2014; Lang et al. 2014), govern propagation of the coronal mass ejections (Lynch et al. 2019), determine the stellar wind pressure exerted on planets (Vidotto et al. 2011, 2013; Garraffo et al. 2016), influence the chemistry and energy balance of the planetary atmospheres (Cohen et al. 2014), and even affect the rocky planet interiors (Kislyakova et al. 2017, 2018). Consequently, characterization of stellar magnetic field has become a staple ingredient of any study of exoplanets orbiting low-mass stars. Consideration of the

magnetic activity is particularly relevant for young systems in which the host star has not yet shed its angular momentum and thus generates more intense magnetic fields than found in older slower rotating M dwarfs.

AU Mic (M1Ve, GJ 803, HD 197481) is one of the nearest and best studied young M dwarfs. It has an age of 22–24 Myr estimated from the membership in the  $\beta$  Pic moving group (Mamajek & Bell 2014; Bell et al. 2015). Due to its proximity ( $d = 9.72 \pm 0.04$  pc, Gaia Collaboration et al. 2018), the circumstellar environment of AU Mic can be spatially resolved with various high-contrast imaging methods. These observations reveal an edge-on debris disk (Kalas et al. 2004; Strubbe & Chiang 2006; Grady et al. 2020) with a complex and dynamic clump structure (Boccaletti et al. 2015, 2018). The transiting planet, AU Mic b, was reported by Plavchan et al. (2020). This Neptune-size planet has an orbital period of 8.46 days and a semimajor axis of about 19 stellar radii. Thus, it is located sufficiently close to the host star to be significantly affected by its magnetic field.

Motivated by these discoveries, here we present a detailed analysis of the surface magnetic field of AU Mic using high-resolution polarimetry and spectroscopy. Our aim is to characterize both the global and small-scale stellar magnetic field components in order to inform future studies of AU Mic and its young planetary system.

## 2. Observational Data

### 2.1. Optical Spectropolarimetry

#### 2.1.1. ESPaDOnS Observations

Several high-resolution circular and linear polarization observations of AU Mic were obtained with the ESPaDOnS instrument (Manset & Donati 2003) at the Canada–France–Hawaii Telescope (CFHT) on Maunakea, Hawaii. These spectra were retrieved from the PolarBase archive (Petit et al. 2014). Four very high-quality Stokes *V* spectra were collected for this star on 2005 July 15–16 using 3600 s exposures for each observation. Three more Stokes *V* spectra were secured on

**Table 1**  
Journal of Circular Polarization Observations of AU Mic

UT Date	HJD	S/N	$\sigma_{\text{LSD}}$	$\langle B_z \rangle$ (G)
ESPaDONs Observations				
2005 Jul 16	2453567.9523	654	3.86e-5	21.2 ± 1.4
2005 Jul 16	2453568.0131	551	4.46e-5	12.8 ± 1.7
2005 Jul 17	2453568.9141	590	4.05e-5	-30.2 ± 1.5
2005 Jul 17	2453569.0061	605	3.90e-5	-27.5 ± 1.5
2006 Aug 02	2453949.9043	466	5.38e-5	46.3 ± 2.0
2006 Aug 02	2453950.0377	527	5.37e-5	69.1 ± 2.0
2006 Aug 03	2453950.9282	480	4.75e-5	34.6 ± 1.7
HARPSpol Observations				
2010 May 03	2455319.8986	188	0.83e-4	5.4 ± 2.2
2010 Aug 08	2455416.8726	91	1.74e-4	53.0 ± 4.6
2010 Aug 09	2455417.8745	44	3.63e-4	-34.4 ± 9.5
2010 Aug 10	2455418.8394	97	1.61e-4	-2.9 ± 4.2
2010 Aug 13	2455421.8552	130	1.17e-4	50.2 ± 3.1

2006 August 2–3, with 4800–7200 s exposure times. Two Stokes  $Q$  and two Stokes  $U$  measurements were also made during the latter observing run using 2400 s exposure times. Also, a single linear polarization measurement, not accompanied by a Stokes  $V$  spectrum, was collected on 2006 May 9. In this case, 2160 s exposure times were employed for Stokes  $Q$  and  $U$  observations.

ESPaDONs spectra cover the 3691–10482 Å wavelength interval and have a resolution of  $R \approx 65\,000$ . The data provided by PolarBase are fully reduced, including continuum normalization. The ESPaDONs observations of AU Mic are characterized by a signal-to-noise ratio (S/N) of 500–600 per  $1.8 \text{ km s}^{-1}$  spectral pixel in the 6000–6500 Å wavelength region. The log of the Stokes  $V$  ESPaDONs observations of AU Mic, including UT observing dates, the heliocentric Julian dates (HJD) of mid-exposure, and individual S/N values, is provided in the upper part of Table 1.

### 2.1.2. HARPSpol Observations

Five circular polarization observations of AU Mic were made with the HARPSpol polarimeter (Piskunov et al. 2011; Snik et al. 2011) attached to the HARPS spectrometer (Mayor et al. 2003) fed by the ESO 3.6 m telescope at La Silla, Chile. One observation was obtained on 2010 May 3. Four more Stokes  $V$  spectra were taken on different nights from 2010 August 8 to August 13. In all cases, an exposure time of 3600 s was used, yielding a median S/N of 44–188 per  $0.8 \text{ km s}^{-1}$  spectral pixel in the 6000–6500 Å wavelength region.

HARPSpol spectra cover the 3780–6913 Å wavelength region, with a small gap around 5300 Å. The resolution is  $R \approx 110\,000$ . The AU Mic observations analyzed here were processed with the REDUCE pipeline (Piskunov & Valenti 2002) as described in detail elsewhere (Makaganiuk et al. 2011a, 2011b). Similar to the ESPaDONs observations described above, each HARPSpol spectropolarimetric measurement comprised four subexposures obtained at different orientations of the quarter-wave retarder wave plate relative to the beamsplitter. The Stokes  $V$  parameter spectrum and the diagnostic null spectrum were derived following the “ratio method” demodulation scheme (Donati et al. 1997; Bagnulo et al. 2009), which allows one to efficiently suppress spurious and instrumental polarization.

Information on individual HARPSpol observations of AU Mic is given in the bottom part of Table 1.

## 2.2. Near-infrared Spectroscopy

### 2.2.1. Y-band Observations

High-resolution spectra of AU Mic in the Y band ( $\lambda$  9640–9790 Å) were employed in this study to measure the mean magnetic field modulus using magnetically sensitive atomic lines. In principle, any ESPaDONs observation described in Section 2.1.1 is suitable for this analysis. However, considering that telluric lines are strong in the region of interest, we made use of the two spectra taken on the night of 2006 May 9 (HJD 2453896.1032 and 2453896.1307) because the telluric absorption was significantly less intense in these observations and was shifted away from the key stellar diagnostic lines. These observations were carried out in the linear polarization mode using 2160 s exposure times.

The data extracted from PolarBase were postprocessed by removing telluric lines. For this purpose, we made use of the slightly adjusted theoretical telluric spectrum calculated by the TAPAS service (Bertaux et al. 2014) for the atmospheric conditions corresponding to the AU Mic observations at CFHT. The final coadded Stokes  $I$  spectrum of AU Mic has  $S/N \approx 500$  per  $1.8 \text{ km s}^{-1}$  pixel in the 9640–9790 Å region.

### 2.2.2. K-band Observations

A measurement of the mean magnetic field of AU Mic was also performed using high-resolution K-band spectra collected with the CRIRES instrument (Kaeuffl et al. 2004) mounted at the 8 m ESO VLT. These observations, carried out on May 8, 2012 (HJD 2456055.9098), cover the 22048–22487 Å wavelength region in four short segments recorded on individual detectors. Here we use only the 22202–22318 Å interval corresponding to the second CRIRES detector. This region contains several magnetically sensitive Ti I lines commonly used for the Zeeman broadening analysis of low-mass stars.

Eight 30 s subexposures acquired at two nodding positions along the slit resulted in  $S/N \approx 700$  per  $1.5 \text{ km s}^{-1}$  pixel in the combined extracted spectrum. The nominal resolving power of these observations, obtained with a slit width of  $0''.2$  and with an adaptive optics system active, is  $R \approx 10^5$ . The CRIRES spectra were reduced with the help of the standard ESO pipeline, as described by, e.g., Shulyak et al. (2014). Similar to the processing of the Y-band data, a custom theoretical telluric spectrum was calculated with TAPAS for the specific atmospheric conditions of the AU Mic observations at VLT. These calculations were first employed to improve the wavelength calibration of the CRIRES spectrum and then to remove telluric spectral features.

## 3. Magnetic Field Analysis

### 3.1. Global Magnetic Field

#### 3.1.1. Least-squares Deconvolution

We applied the least-squares deconvolution (LSD, Donati et al. 1997; Kochukhov et al. 2010) multiline technique to derive high-quality mean circular and linear polarization profiles from the ESPaDONs and HARPSpol observations of AU Mic. To this end, we made use of the iLSD code described by Kochukhov et al. (2010). The line mask required by this

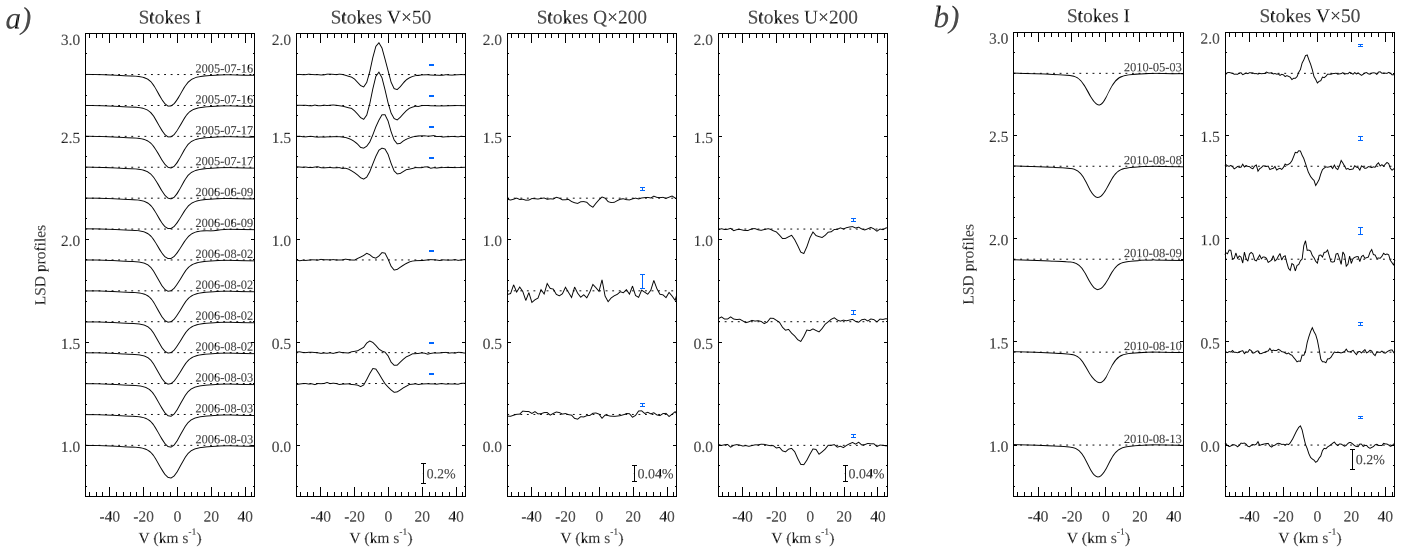


**Figure 1.** LSD Stokes parameter profiles of AU Mic derived from ESPaDOnS (a) and HARPSpol (b) spectropolarimetric observations. Profiles corresponding to different observations are shifted vertically. The polarization profiles are scaled up relative to Stokes  $I$  by the factors indicated above each panel.

software was constructed from an atomic line list retrieved from the VALD database (Ryabchikova et al. 2015) with the atmospheric parameters  $T_{\text{eff}} = 3700$  K and  $\log g = 4.5$ . We retained only lines deeper than 20% of the continuum and excluded regions affected by telluric absorption. Stellar lines significantly deviating from the average shape (e.g., emission lines, strong metal lines with broad wings) were also excluded. The final mask contained 5331 lines for ESPaDOnS (mean wavelength  $\lambda_0 = 5800$  Å, mean effective Landé factor  $z_0 = 1.2$ ) and 5108 lines for HARPSpol spectra ( $\lambda_0 = 5300$  Å,  $z_0 = 1.2$ ). The resulting typical error bar (polarimetric sensitivity) was  $5 \times 10^{-5}$  per  $1.8 \text{ km s}^{-1}$  velocity bin for the ESPaDOnS LSD profiles and  $10^{-4}$  per  $1.0 \text{ km s}^{-1}$  bin for the LSD profiles derived from HARPSpol observations (see column 4 in Table 1).

With this multiline analysis we have succeeded in detecting circular polarization signatures with an amplitude of 0.1–0.3% relative to the Stokes  $I$  continuum in all 12 Stokes  $V$  observations of AU Mic. Moreover, linear polarization signals with an amplitude of 0.05% were systematically detected in the ESPaDOnS Stokes  $U$  observations. These signatures appear to have approximately constant shape and amplitude. One marginal polarization signature, with an amplitude less than 0.02%, was also detected in the Stokes  $Q$  spectrum from May 6, 2009. Two other Stokes  $Q$  observations showed no signatures associated with the stellar photospheric spectrum.

All LSD Stokes parameter profiles of AU Mic are illustrated in Figure 1. There is significant variability of both the shape and amplitude of the Stokes  $V$  profiles. On the other hand, the Stokes  $U$  profile is largely stationary. The seven ESPaDOnS Stokes  $V$  observations come in three batches separated by 2–11 months. Each group covers at most two consecutive nights at a time. It is difficult to tell from these data if the observed variation of the Stokes  $V$  profiles is due to rotational modulation or caused by a long-term magnetic activity cycle. The HARPSpol data set is more informative in this respect. The four Stokes  $V$  profiles corresponding to the observations obtained on 2010 August 8–13, (Figure 1b) exhibit significant variability and include all basic profile shape types seen in the ESPaDOnS data set. This indicates that the observed Stokes  $V$

profile changes are likely explained by the rotational modulation and that the global field topology of AU Mic is dominated by a nonaxisymmetric component.

Interestingly, some of the strongest circular polarization profiles in both data sets (July 16–17, 2005 for ESPaDOnS, 2010 May 3 and August 10 for HARPSpol) correspond to the symmetric, W-shaped Stokes  $V$  profiles. This so-called crossover signature (Mathys 1995) is explained by the presence of a pair of regions with opposite magnetic polarity at the approaching and receding stellar hemispheres, which again suggests a nonaxisymmetric large-scale field geometry. The other Stokes  $V$  profiles exhibit the classical antisymmetric S-shape corresponding to a positive line-of-sight magnetic field component. One HARPSpol Stokes  $V$  spectrum (2010 August 9) shows a weak negative circular polarization signature. The HARPSpol observations obtained five nights apart (2010 August 8 and August 13) yield very similar Stokes  $V$  LSD profiles, which is consistent with recent estimates of the stellar rotation period  $P_{\text{rot}} \approx 4.85$  days (Ibañez Bustos et al. 2019; Plavchan et al. 2020).

We quantified the strength of the disk-averaged line-of-sight (longitudinal) magnetic field  $\langle B_z \rangle$  by computing the first moment of the Stokes  $V$  profile and normalizing by the equivalent width of the Stokes  $I$  profile (Kochukhov et al. 2010). The measurement window of  $\pm 20 \text{ km s}^{-1}$  from the mean radial velocity of AU Mic was adopted. This analysis yielded 12  $\langle B_z \rangle$  measurements reported in the last column of Table 1. We found longitudinal field in the range from  $-34$  to  $69$  G, with typical error bars of 1.5–2 G for ESPaDOnS and 2–9 G for HARPSpol data. Note that although  $\langle B_z \rangle$  is formally compatible with zero for the HARPSpol observations on 2010 May 3 and August 10, the crossover LSD polarization signatures are still detected unambiguously on both nights.

The diagnostic null spectra were processed with the same LSD approach applied to the Stokes  $V$  and Stokes  $QU$  observations. No polarization signatures were detected in any of the null LSD profiles. This confirms that the line polarization signatures found for AU Mic are likely to be of stellar origin and are not significantly affected by instrumental artifacts. The basic difference in shape of the symmetric Stokes  $U$  signal from the antisymmetric Stokes  $V$  profile corresponding to the

data obtained on the same nights indicates that the Stokes  $U$  signature could not have been produced by a cross-talk from Stokes  $V$ .

The three-lobe morphology of the Stokes  $U$  signature, clearly discernible in two out of three linear polarization observations, is qualitatively consistent with the profile shape expected for the Zeeman effect for a line with triplet magnetic splitting. Comparison of the Stokes  $U$  LSD profiles calculated using subsets of lines with different magnetic sensitivity shows that the linear polarization amplitude correlates with the effective Landé factor. This reinforces the conclusion that the observed Stokes  $U$  signature originates from the Zeeman effect and is linked to the stellar magnetic field.

### 3.1.2. Zeeman Doppler Imaging

Considering the scatter of recent determinations of the rotation period of AU Mic (Ibañez Bustos et al. 2019; Plavchan et al. 2020), we estimate its precision to be approximately 0.01–0.02 days. This uncertainty, together with the possibility of intrinsic changes of the surface magnetic field geometry, precludes modeling of the entire collection of AU Mic spectropolarimetric observations within a single framework. The five HARPSpol spectra taken in 2010 over about 100 days are better suited for that purpose. Therefore, in this section we interpret these data with the Zeeman Doppler imaging (ZDI, Kochukhov 2016) technique. Due to the sparseness of the rotational phase coverage, the HARPSpol observations are hardly sufficient for deriving a robust global magnetic field model. Nevertheless, we attempted to reproduce these five Stokes  $V$  profiles with the ZDI code InversLSD (Kochukhov et al. 2014) in order to get a rough idea about the structure and strength of the global magnetic field of AU Mic.

The ZDI analysis was carried for AU Mic similar to previous applications of InversLSD to G, K, and M stars (Kochukhov 2015; Hackman et al. 2016; Rosén et al. 2016; Lavail et al. 2018). The local Stokes parameter profiles were approximated with the Unno–Rachkovsky analytical solution of the polarized radiative transfer equation (e.g., Landi Degl’Innocenti & Landolfi 2004). The line strength and broadening parameters were adjusted to match the Stokes  $I$  LSD profile. The projected rotational velocity  $v_e \sin i$  of  $9.17 \text{ km s}^{-1}$  was used according to the results of Section 3.2 and the inclination angle of the stellar rotational axis was set to  $90^\circ$ , consistent with the observation of spin–orbit alignment (Martoli et al. 2020) and the edge-on orientation of the debris disk (Watson et al. 2011; Greaves et al. 2014).

The first HARPSpol observation in the series was taken about 20 stellar rotations prior to the remaining four Stokes  $V$  observations. In this case, a period error of 0.01–0.02 days incurs about 0.2–0.4 uncertainty of the rotational phase. This necessitates adjusting the rotational period to achieve a better match to the spectropolarimetric observations, as commonly practiced by ZDI studies of M dwarfs (Donati et al. 2008b; Morin et al. 2008). We found that  $P_{\text{rot}} = 4.88 \text{ d}$  minimizes the chi-square of the fit to Stokes  $V$  profiles. This value of the rotational period, reasonably consistent with other determinations, was adopted for the final magnetic inversion.

Similar to other modern applications of ZDI, we represented the stellar magnetic field topology with a spherical harmonic expansion (Kochukhov et al. 2014) that included both poloidal and toroidal terms. The expansion was truncated at the angular degree  $\ell_{\text{max}} = 5$ . However, the equator-on orientation of

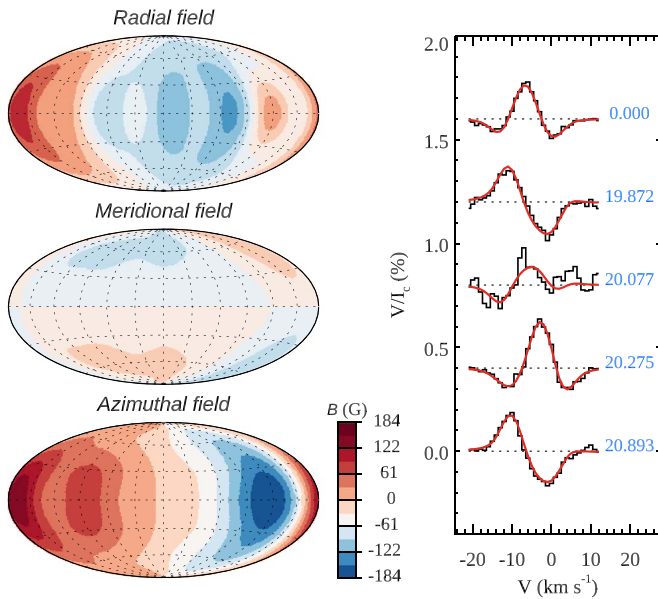
AU Mic leads to several degeneracies in applications of surface mapping techniques. Specifically, for the spherical harmonic global field description adopted in our study, the contribution of any axisymmetric harmonic mode that is antisymmetric with respect to the stellar equator (i.e., any odd- $\ell$ ,  $m = 0$  spherical harmonic) is canceled out in circular polarization observables independently of the quality of observations and rotational phase coverage. This means that contributions of these field components, including a dipole aligned with the stellar rotational axis, cannot be determined from Stokes  $V$  observations.

Figure 2 presents results of our tentative ZDI modeling. The magnetic field maps reveal a distinctly nonaxisymmetric field structure, with the local field strength reaching 184 G. The average global field strength is 88 G. The harmonic decomposition of the field indicates that the poloidal component dominates over the toroidal one (91.2% of the magnetic field energy is in the poloidal field) and that the large-scale field is almost entirely nonaxisymmetric (96.0% of the magnetic energy is in  $|m| \geq \ell/2$  modes). The dipolar modes contribute 70.2% of the magnetic energy. These quantitative characteristics of the global magnetic field of AU Mic are summarized in the upper part of Table 2.

### 3.1.3. Constraints on Axisymmetric Field Component

A nonaxisymmetric global magnetic field structure of AU Mic inferred from the qualitative analysis of Stokes  $V$  profiles and suggested by the preliminary ZDI map may be incomplete due to two separate issues. First, the phase coverage of the HARPSpol spectropolarimetric data is sparse and some surface structures might have been missed owing to a large phase gap between observations corresponding to the rotational phases 0.27 and 0.87 s, and our magnetic inversion suffers from a more fundamental limitation. For the stellar inclination  $i \approx 90^\circ$ , any field component with opposite field polarities above and below the stellar equator, e.g., a dipole aligned with the rotational axis, will not produce a measurable circular polarization. However, this degeneracy can be alleviated with the help of linear polarization observations. A comparison of linear and circular polarization is meaningful only if the measurements are done almost simultaneously. Fortunately, two complete Stokes  $VQU$  sequences were obtained for AU Mic on 2006 August 2–3. Based on the LSD profiles corresponding to these full Stokes vector spectra we conclude that the ratio of the maximum absolute Stokes  $V$  amplitude  $|V|_{\text{max}}$  to the maximum total linear polarization  $(P_L)_{\text{max}} \equiv (\sqrt{Q^2 + U^2})_{\text{max}}$  is 2.3–3.1. One can use this measurement to assess the strength of the axisymmetric dipolar field that cannot be diagnosed with Stokes  $V$  alone.

Figure 3 shows a series of forward five Stokes parameter calculations with InversLSD for the same four rotational phases of HARPSpol spectra modeled with ZDI in the previous section. This figure compares synthetic  $V$  and  $P_L$  profiles computed for the original nonaxisymmetric global field map (Figure 2) with the calculations for the maps in which the  $\ell = 1$ ,  $m = 0$  harmonic component was set to  $B_{1,0} = 1, 2,$  and  $3 \text{ kG}$ . In accordance with the discussion above, this modification has no influence on Stokes  $V$ , but linear polarization increases with  $B_{1,0}$ . The observed  $|V|_{\text{max}} / (P_L)_{\text{max}}$  ratio is reproduced with a dipolar field strength of 1.3–2.7 kG. Considering only the HARPSpol spectra for the rotational phases 0.872 and 0.893 (2010 August 8 and 13), which exhibit



**Figure 2.** Results of the ZDI fit to the five HARPSpol Stokes  $V$  observations of AU Mic obtained in August 2010. The radial, meridional, and azimuthal magnetic field maps are displayed on the left using the Hammer-Aitoff projection. Comparison of the observed (histogram) and model (solid lines) circular polarization spectra is presented on the right. The profiles corresponding to different observing dates are offset vertically. Rotational phases are calculated with the ephemeris  $\text{HJD} = 2455319.8986 + 4.88 \times E$ .

**Table 2**  
Magnetic Field Characteristics of AU Mic

Parameter	Value
Global magnetic field from LSD Stokes $V$	
$\langle B_V \rangle$ (kG)	0.088
$E_{\text{pol}}$ (%)	91.2
$E_{\ell=1}$ (%)	70.2
$E_{ m  \geq \ell/2}$ (%)	96.0
Axisymmetric dipolar field from LSD Stokes $QU$	
$B_d$ (kG)	1.8–2.2
Mean field modulus from $Y$ -band Ti I lines	
$\langle B \rangle$ (kG)	$2.31 \pm 0.05 (\pm 0.2)$
$\log(N_{\text{Ti}}/N_{\text{tot}})$	$-7.06 \pm 0.01$
$v_e \sin i$ (km s $^{-1}$ )	$9.17 \pm 0.12$
Mean field modulus from $K$ -band Ti I lines	
$\langle B \rangle$ (kG)	$2.08 \pm 0.02 (\pm 0.2)$
$\log(N_{\text{Ti}}/N_{\text{tot}})$	$-7.08 \pm 0.01$
$v_e \sin i$ (km s $^{-1}$ )	$9.24 \pm 0.11$

**Note.** The error bars given for  $\langle B \rangle$  in brackets indicate systematic uncertainties.

very similar Stokes  $V$  signatures in comparison to 2006 August 2–3 ESPaDOnS observations, we can reduce this range to  $B_{1,0} = 1.8\text{--}2.2$  kG. Thus, we find it plausible that AU Mic possesses a fairly strong axisymmetric dipolar field in addition to the nonaxisymmetric large-scale field of the type illustrated in Figure 2.

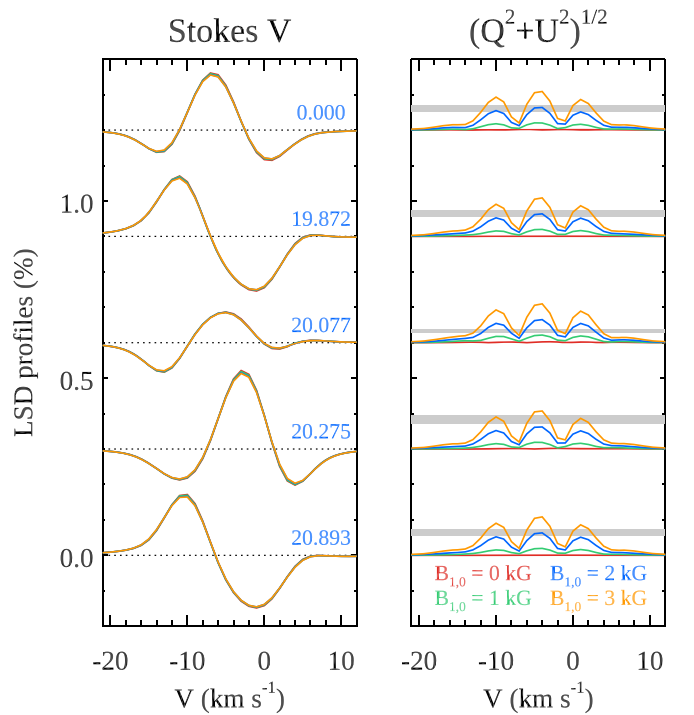


**Figure 3.** Theoretical Stokes  $V$  (left) and total linear polarization  $P_L = \sqrt{Q^2 + U^2}$  (right) LSD profiles for different strengths of the axisymmetric dipolar field component. The profiles corresponding to different rotation phases are offset vertically. The horizontal gray bar in the right panel shows the observed linear polarization amplitude estimated from the ESPaDOnS Stokes  $QU$  observations.

## 3.2. Mean Field Modulus

### 3.2.1. $Y$ -band Analysis

Previous studies (Kochukhov & Lavail 2017; Kochukhov & Shulyak 2019; Shulyak et al. 2017, 2019) have established the group of 10 Ti I lines at  $\lambda 9647.37\text{--}9787.69$  Å as a very useful indicator of magnetic fields in low-mass main sequence stars. These neutral titanium lines belong to the same multiplet, which eliminates uncertainty of their modeling stemming from oscillator strength errors and ensures that they form under similar thermodynamic conditions in stellar atmospheres. These lines exhibit a widely different response to a magnetic field. Several of them (e.g.,  $\lambda 9647.37$ ,  $9688.87$ ,  $9770.30$ , the blend of  $9783.31$  and  $9783.59$ , and  $9787.69$  Å) are noticeably strengthened and broadened by the Zeeman effect, whereas other lines are affected to a lesser extent. This multiplet includes an exceptionally rare magnetic null line  $\lambda 9743.61$  Å that has a zero Landé factor and can be used to constrain Ti abundance and nonmagnetic broadening.

Our analysis of the  $Y$ -band Ti I lines in the spectrum of AU Mic followed the methodology described by Shulyak et al. (2014, 2017) and Kochukhov & Lavail (2017). We calculated theoretical intensity spectra with the help of the polarized radiative transfer code SYNMAST (Kochukhov et al. 2010) assuming a uniform radial magnetic field. The line list for these calculations was obtained from the VALD database (Ryabchikova et al. 2015) with the van der Waals damping parameters calculated according to Barklem et al. (2000). A solar metallicity MARCS (Gustafsson et al. 2008) model atmospheres with  $T_{\text{eff}} = 3700$  K (Houdebine et al. 2016; Afram & Berdyugina 2019; Plavchan et al. 2020) and  $\log g = 4.5$  cm s $^{-2}$

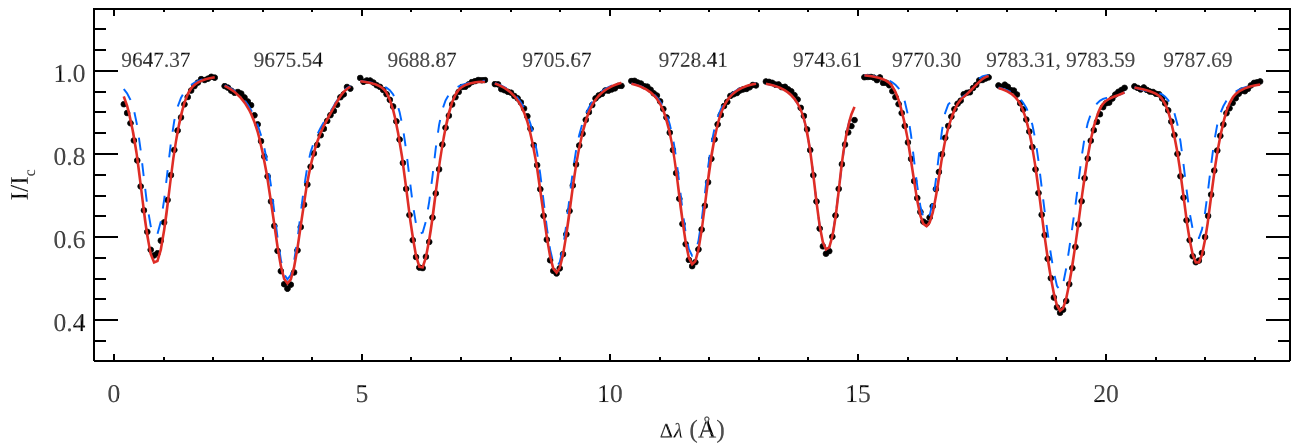


**Figure 4.** Comparison of the observed (symbols) and computed (lines) profiles of nine near-infrared Ti I lines in the Y-band spectrum of AU Mic. The solid line shows the best-fit magnetic model spectrum. The dashed line illustrates theoretical profiles calculated without a magnetic field. The central wavelength of each transition, in Å units, is indicated above the corresponding line profile.

was used. This surface gravity is close to the  $\log g$  range 4.39–4.48 implied by different estimates of the stellar mass and radius given by Plavchan et al. (2020). The microturbulent velocities are known to be relatively weak in M-dwarf atmospheres. Here we adopted  $\xi_t = 0.25 \text{ km s}^{-1}$  according to the calibration provided by the three-dimensional hydrodynamic simulations by Wende et al. (2009).

Several previous Zeeman broadening analyses of M dwarfs (Johns-Krull & Valenti 1996, 2000; Shulyak et al. 2017, 2019) have demonstrated the need of multicomponent field strength distributions for achieving satisfactory line-profile fits. Here we approximated this distribution by a combination of  $B = 0, 2,$  and  $4 \text{ kG}$  spectral components, added with the filling factors  $f_0, f_2,$  and  $f_4$  ( $f_0 + f_2 + f_4 = 1$ ). The filling factor  $f_i$  represents the fraction of the stellar surface occupied by the field  $B_i$ . The same model atmosphere was used for calculating spectral contributions of all three components. Similar field strength distribution parameterizations are commonly used by the Zeeman broadening studies of M dwarfs and T Tauri stars (Johns-Krull et al. 1999; Johns-Krull & Valenti 2000; Johns-Krull 2007; Yang et al. 2008; Yang & Johns-Krull 2011; Lavail et al. 2019). In our case, the free parameters fitted to the observed Ti I line profiles include the Ti abundance, the projected rotational velocity  $v_e \sin i$ , the radial velocity  $V_r$ , and the two filling factors  $f_2$  and  $f_4$ . The individual continuum scaling factors were also allowed to vary in order to compensate small continuum normalization errors (e.g., Shulyak et al. 2017). The field-free filling factor  $f_0 = 1 - f_2 - f_4$  and the mean field modulus  $\langle B \rangle \equiv \sum B_i f_i = 2 \cdot f_2 + 4 \cdot f_4$  are dependent parameters derived from  $f_2$  and  $f_4$ .

The parameter optimization was carried out with the help of the Markov chain Monte Carlo (MCMC) sampling algorithm implemented in the SoBAT set of routines (Anfinogentov et al. 2020) written in IDL. The advantage of using a MCMC method compared to the traditional least-squares fitting is the possibility of incorporating prior constraints (e.g., the requirements  $0 \leq f_i \leq 1$  and  $\sum f_i = 1$ ) through a rigorous Bayesian approach and obtaining robust error bars that account for all relevant parameter correlations. In this analysis of AU Mic we ran the MCMC walkers for  $10^5$  steps after the initial  $10^4$  step burn-in stage. Uniform priors were assigned on each parameter. The best-fit parameter values were calculated as the median of

the posterior distributions. The error bars were obtained from the same distributions, using the 68% confidence interval.

Our final theoretical fit to the Ti I lines in the Y-band spectrum of AU Mic is shown in Figure 4. There is a clear evidence of both Zeeman broadening and magnetic intensification, with the Ti I  $\lambda 9688.87 \text{ Å}$  line showing the strongest effect. The marginalized posterior distributions of independently fitted parameters are shown in Figure 5. The corresponding distributions are illustrated in Figure 6 for the dependent parameters  $f_0$  and  $\langle B \rangle$ . Both of these plots were produced with the help of the Corner Python package (Foreman-Mackey 2016). The marginalized posterior distributions reveal several significant parameter correlations such as, for example, between  $f_2$  and  $f_4$  and between both filling factors and  $v_e \sin i$  (Figure 5). These correlations would normally be ignored by classical least-squares fits, leading to underestimated uncertainties. The correlation of filling factors suggests that using a finer grid of independently fitted magnetic components is not justified by the data. We have also verified that adding a  $B = 6 \text{ kG}$  component does not result in a perceptible improvement of the fit quality and is not supported by the formal criteria, such as the Bayesian Information Criterion (Sharma 2017).

The results of our spectrum synthesis analysis of the Y-band Ti I lines are summarized in the middle section of Table 2. Specifically, we found the mean field modulus  $\langle B \rangle = 2.31 \pm 0.05 \text{ kG}$ . These relatively tight error bars correspond to the formal fitting errors obtained using a fixed set of model atmosphere parameters and a particular field strength parameterization. We estimated the systematic uncertainties by repeating the MCMC parameter inference, changing  $T_{\text{eff}}$  by  $\pm 100 \text{ K}$ ,  $\log g$  by  $\pm 0.1 \text{ dex}$ , and  $\xi_t$  by  $\pm 0.25 \text{ km s}^{-1}$ . We also studied the effect of choosing a different field strength parameterization by using a three-component model with  $B = 1, 3,$  and  $5 \text{ kG}$  (e.g., Johns-Krull et al. 1999). The outcome of this series of tests showed that  $\langle B \rangle$  can increase by up to  $0.2 \text{ kG}$  and can be reduced by  $0.1 \text{ kG}$ , whereas other parameters remain consistent within the error bars with the values reported in Table 2.

The projected rotational velocity derived here is somewhat smaller than the  $v_e \sin i = 9.3\text{--}9.7 \text{ km s}^{-1}$  estimated by Torres et al. (2006) and Houdebine (2010). This difference is to be expected since we account for Zeeman broadening in our

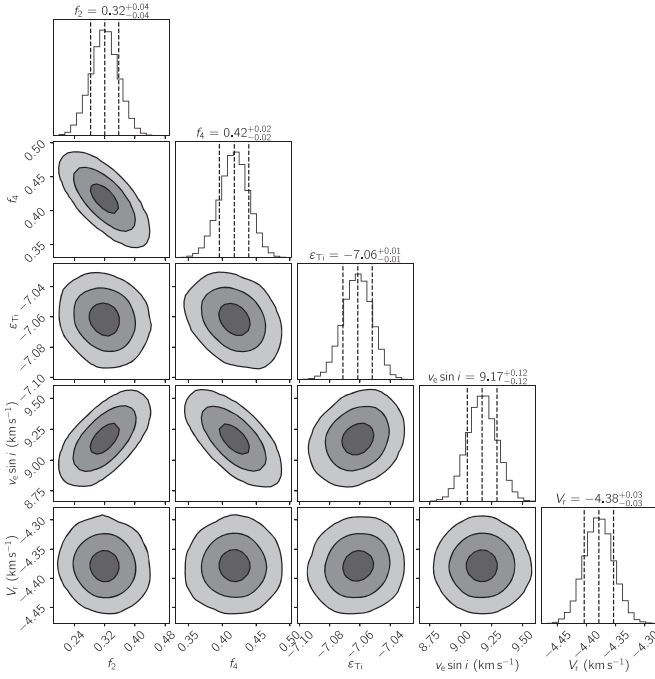


**Figure 5.** Marginalized posterior distributions of independent parameters fitted to the *Y*-band Ti I lines. Contours correspond to  $1\sigma$ ,  $2\sigma$ , and  $3\sigma$  confidence levels.

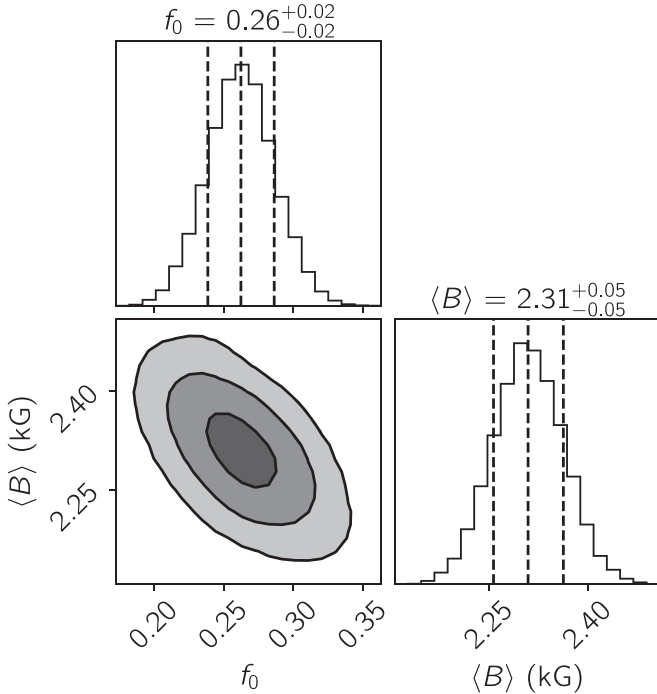


**Figure 6.** Marginalized posterior distributions of the filling factor of field-free regions  $f_0$  and the mean field modulus  $\langle B \rangle$  derived from the *Y*-band Ti I lines.

spectroscopic modeling. On the other hand, one can obtain  $v_e = 7.8 \pm 0.3 \text{ km s}^{-1}$  from  $P_{\text{rot}}$  and interferometric measurement of the stellar radius  $R = 0.75 \pm 0.03 R_{\odot}$  (White et al. 2019). This is smaller than any spectroscopic values of  $v_e \sin i$  reported for AU Mic in the literature. This discrepancy might be explained by a contribution of another broadening mechanism such as, for example, enhanced macroturbulence, to the line profiles of this star. We have verified that our best-

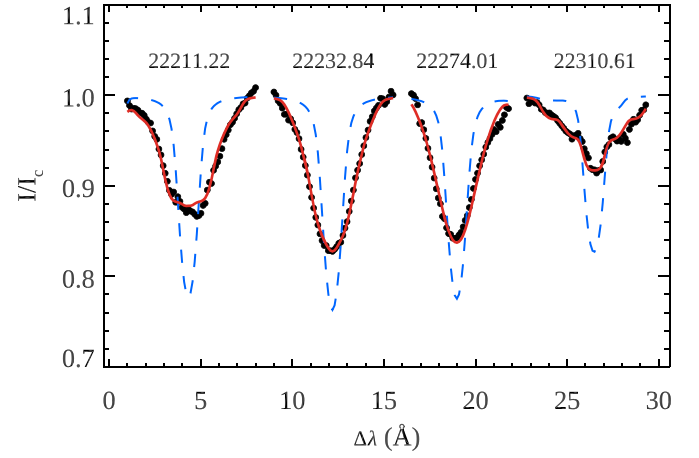


**Figure 7.** Same as Figure 4, but for the *K*-band Ti I lines.

fitting  $v_e \sin i$  can be reduced down to  $8.1 \text{ km s}^{-1}$  if the radial-tangential macroturbulent broadening  $\zeta_t \approx 4.5 \text{ km s}^{-1}$  is assumed for the analysis of Ti I lines. Nevertheless, this has no impact on the derived mean magnetic field strength or the filling factors of individual magnetic components.

### 3.2.2. *K*-band Analysis

We carried out a spectrum synthesis analysis of the CRIRES *K*-band observation of AU Mic with the same procedure as applied above. Considering temporal variability associated with rotational modulation and intrinsic changes of the surface magnetic field that might have occurred during six years separating ESPaDOnS and CRIRES observations, and possible formation depth difference of the spectral diagnostics, we analyze atomic lines in the *Y* and *K* bands independently. Due to the limited wavelength coverage of the *K*-band spectrum, only four neutral titanium spectral lines,  $\lambda$  22211.22, 22232.84, 22274.01, and 22310.61 Å, are available for modeling. All these spectral features have large effective Landé factors (1.6–2.1 for the first three lines and 2.5 for Ti I 22310.61 Å) and are significantly affected by a kG-strength magnetic field. Owing to a lack of suitable magnetically insensitive lines in the observed wavelength region, we fitted the *K*-band spectrum with a Gaussian prior on  $v_e \sin i$  according to the results of Section 3.2.1.

Figure 7 shows comparison of the observed Ti line profiles with the best-fit theoretical model. The magnetic broadening and profile distortion of the studied spectral lines are clearly evident, particularly for the Ti I 22310.61 Å line. The marginalized posterior distributions of  $f_0$  and  $\langle B \rangle$  obtained with the MCMC sampling are shown in Figure 8. The *K*-band analysis results are reported in the bottom part of Table 2.

The CRIRES spectrum yields  $\langle B \rangle = 2.08 \pm 0.02 \text{ kG}$ . This estimate of the mean field modulus is not affected by possible errors of  $T_{\text{eff}}$ ,  $\log g$ , and  $\zeta_t$ . At the same time,  $\langle B \rangle$  increases to  $2.32 \pm 0.04 \text{ kG}$  if the fitted field strength distribution is changed from  $B = 0, 2, 4 \text{ kG}$  to  $B = 1, 3, 5 \text{ kG}$ . This indicates a systematic error of  $\approx 0.2 \text{ kG}$  for  $\langle B \rangle$ . The filling factor of nonmagnetic regions,  $f_0 = 0.23 \pm 0.01$ , derived from the *K*-band Ti I lines in the framework of the former field strength distribution model, agrees with the *Y*-band results ( $f_0 = 0.26 \pm 0.02$ ). Likewise, we found no improvement of the fit quality when the field strength distribution was extended to include the  $B = 6 \text{ kG}$  component.

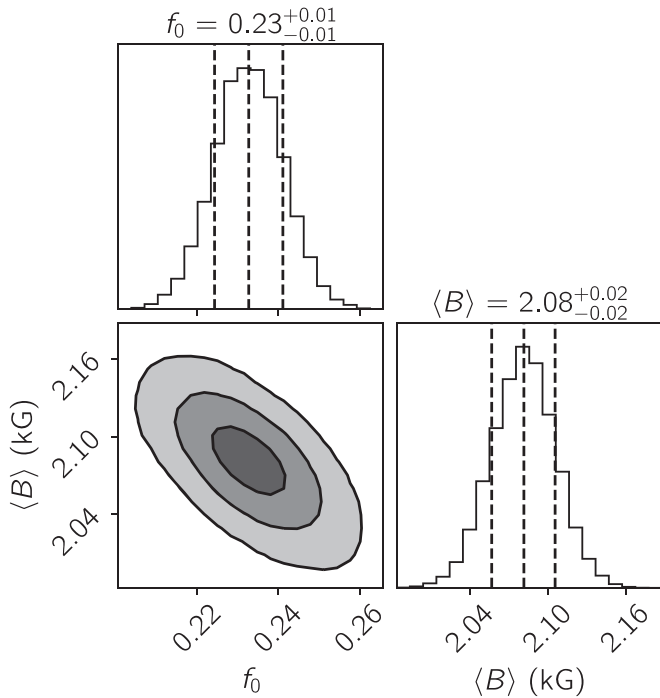


Figure 8. Same as Figure 6, but for the analysis based on the *K*-band Ti I lines.

#### 4. Discussion

In this paper we presented a comprehensive analysis of the surface magnetic field of the young M-dwarf star AU Mic. We studied both the polarization diagnostics linked to the large-scale stellar magnetic field and the Zeeman broadening and intensification of intensity line profiles, which captures the total magnetic flux. Using high-resolution Stokes parameter observations collected with two different spectropolarimeters, we systematically detected circular polarization in the photospheric line profiles with the help of the LSD multiline technique. We reported 12 mean longitudinal magnetic field measurements spanning the range from  $-34$  to  $69$  G. These measurements correspond to the spectra acquired on nine individual nights during two observing epochs (2005–2006 and 2010) separated by about four years. No qualitative change of the characteristics of the global field of AU Mic, such as changes of the Stokes *V* profile morphology or magnitude of  $\langle B_z \rangle$ , was found between these two epochs. The only other longitudinal field measurement available for AU Mic was recently obtained by Martioli et al. (2020) based on near-infrared spectropolarimetric observations carried out in 2019 June. These authors derived  $\langle B_z \rangle = 46$  G, which is in agreement with the  $\langle B_z \rangle$  range of our optical measurements. The circular polarization profiles of AU Mic exhibit a strong rotational modulation, alternating in shape from symmetric to antisymmetric. This shape variation, and the mere presence of symmetric crossover Stokes *V* profiles, suggests a nonaxisymmetric global magnetic field topology.

We also detected a linear polarization signal in the photospheric line profiles of AU Mic. This signal manifested as a nearly stationary signature in Stokes *U*. The shape of this signature and its dependence on the spectral line parameters indicates that it arises due to the Zeeman effect. Weak linear polarization was previously detected in the active M dwarf AD Leo (Lavail et al. 2018) and a few other more massive active late-type stars (Kochukhov et al. 2011; Rosén et al.

2013). These studies reported the ratio of the Stokes *V* to Stokes *QU* amplitude to be about 5–13. Here we found a much smaller ratio of 2–3, making linear polarization of AU Mic unusually strong for the Stokes *V* signal observed in this star. This may be due to the equator-on orientation of the star, which facilitates cancellation of the circular polarization signatures produced by any global field component antisymmetric with respect to the stellar equator.

A preliminary ZDI analysis based on the subset of Stokes *V* profiles collected in 2010 reveals a weak nonaxisymmetric magnetic field configuration with a peak field strength of 184 G and a mean field strength of  $\langle B_V \rangle = 88$  G. These global field characteristics of AU Mic are similar to some of the fields reconstructed with ZDI for early-M dwarfs (Donati et al. 2008b; Kochukhov & Shulyak 2019), although a combination of the dominant poloidal field with a large degree of non-axisymmetry of this field component is relatively uncommon in these stars.

Consideration of linear polarization completely changes our perspective on the global magnetic field of AU Mic. We showed that the large linear-to-circular polarization amplitude ratio observed for this star can be reproduced by adding  $\approx 2$  kG axisymmetric dipolar field to the ZDI map reconstructed from Stokes *V* profiles. This field component is not observed in circular polarization due to the cancellation effect but gives rise to an observable linear polarization. The presence of a strong axisymmetric dipolar field makes magnetic field configuration of AU Mic more similar to the large-scale fields found in mid- and late-M dwarfs (Morin et al. 2008, 2010) or to the fields of T Tauri stars with small radiative cores (Donati et al. 2008a, 2010). The latter similarity is probably not too surprising given the youth of AU Mic and its pre-main-sequence evolutionary status (Plavchan et al. 2020).

The problem of underestimation of the strength of axisymmetric magnetic field component is not specific to our ZDI analysis of AU Mic but, in principle, affects any Stokes *V* investigation of an equator-on star. For this cancellation effect to be significant, the stellar inclination angle must be close to  $90^\circ$ . This situation is rare for a random star but common for transiting exoplanet hosts (Fares et al. 2010) and detached eclipsing binaries (Kochukhov & Shulyak 2019). Thus, interpretation of ZDI results obtained for these objects should take into account the possible presence of a strong axisymmetric field not captured by the circular polarimetric diagnostics.

Our analysis of the global field topology of AU Mic is based on a data set with a rather sparse phase coverage and therefore should be considered preliminary. It can be significantly improved with the help of new full Stokes vector observations with a dense phase coverage. We emphasize that linear polarization spectra provide information on the large-scale field of this star that should not be neglected. Future ZDI investigations will have to incorporate the Stokes *Q* and *U* data in the magnetic inversions in order to provide a complete characterization of the global field of AU Mic.

Polarimetric investigation of the global magnetic field of AU Mic was complemented by the measurement of the mean field modulus from intensity spectra. This analysis provides information on the total magnetic field of the star, including the small-scale magnetic component that cannot be assessed with polarimetric methods. We applied detailed magnetic spectrum synthesis modeling to the two groups of near-infrared Ti I lines

located in the  $Y$  and  $K$  bands. From the first set of lines we inferred  $\langle B \rangle = 2.3 \pm 0.2$  kG, whereas the second set yielded  $\langle B \rangle = 2.1 \pm 0.2$  kG. In both cases, the best description of the observed line profiles was achieved by combining at least three spectral contributions corresponding to magnetic fields ranging from 0 to 4 kG in strength. In the context of this modeling approach, we inferred that about 23–26% of the stellar surface is field-free.

Two previous studies analyzed Zeeman broadening in AUMic spectra with a two-component approach, which assumes that a fraction  $f$  of the stellar surface is covered by the field  $B$  and the rest is nonmagnetic. Saar (1994) measured  $\langle B \rangle = Bf = 2.3$  kG from  $K$ -band Fourier transform spectra, in excellent agreement with our results. On the other hand, Afram & Berdyugina (2019) determined  $\langle B \rangle = 3.2$ – $3.4$  kG from different sets of atomic and molecular lines in the optical. Their selection of atomic lines included three Ti I transitions at  $\lambda$  8364–8385 Å with parameters similar to the  $Y$ -band titanium lines studied in our paper. The authors estimated the error of their measurement to be about 0.6 kG, making these results incompatible with the outcome of our study. The analysis by Afram & Berdyugina (2019) relied on one of the ESPaDOnS spectra (July 16, 2005) studied in Section 3.1.1. Although we used a different ESPaDOnS observation from 2006 for the  $Y$ -band  $\langle B \rangle$  determination, direct comparison of these two spectra reveals no difference of the strengths and/or shapes of the Ti I lines at  $\lambda$  9640–9790 Å employed in our work. Thus, the discrepant field strength measurement reported by Afram & Berdyugina (2019) cannot be attributed to intrinsic variation of the star.

The mean field modulus derived by us for AUMic coincides with  $\langle B \rangle = 2.2$  kG, suggested by Cranmer et al. (2013) based on the field equipartition arguments. This lends support to the model of turbulent coronal heating developed by these authors to explain X-ray, radio, and millimeter observations of AUMic.

Comparison of the mean global field strength estimated from the tentative Stokes  $V$  ZDI with the mean field modulus inferred from Zeeman broadening suggests that most of the magnetic field energy of AUMic is concentrated on small scales. The ratio  $\langle B_V \rangle / \langle B \rangle \approx 4\%$  is typical of early-M dwarfs with weak, complex large-scale fields (Kochukhov & Shulyak 2019). However, the 2 kG axisymmetric dipolar field favored by the linear polarization data implies the disk-averaged global field of  $\langle B_{\text{QU}} \rangle \approx 1$  kG and  $\langle B_{\text{QU}} \rangle / \langle B \rangle \approx 46\%$ . This ratio of the global-to-total field strength is unusually high for an M dwarf but has been observed for some T Tauri stars (Lavail et al. 2019).

The information on the magnetic field of AUMic provided in this study will be essential for analyses of star–planet magnetic interaction and for modeling stellar forcing on the planetary atmosphere. Given the planet’s orbital distance of  $\approx 19$  stellar radii, it is likely located beyond the Alfvén surface. This makes detailed MHD stellar wind simulations (e.g., Vidotto et al. 2013; Cohen et al. 2014) necessary for estimating the pressure exerted by the stellar wind and extended magnetosphere on the planet. Such simulations are enabled by the constraints on global magnetic field reported here. On the other hand, accurate measurement of the total magnetic flux constrains coronal heating and wind acceleration due to Alfvén wave turbulence (Garraffo et al. 2016).

We thank Lisa Rosén for her contribution to the reduction and preliminary analysis of the HARPSpol observations of AUMic and Mathias Zechmeister for reducing the CRIRES spectrum of this star. We also thank Paul Barklem for calculating the van der Waals damping parameters for the spectral lines studied in this paper.

This study was supported by the Swedish Research Council and the Swedish National Space Agency. This work is based on observations collected at the European Southern Observatory (programs 85.D-0296 and 89.C-0173); and based on observations obtained at the CFHT which is operated by the National Research Council of Canada, the Institut National des Sciences de l’Univers (INSU) of the Centre National de la Recherche Scientifique (CNRS) of France, and the University of Hawaii.

This work has made use of the VALD database, operated at Uppsala University, the Institute of Astronomy RAS in Moscow, and the University of Vienna.

*Facilities:* ESO:3.6 m (HARPSpol), ESO:VLT (CRIRES), CFHT (ESPaDOnS).

*Software:* REDUCE (Piskunov & Valenti 2002), iLSD and SYNMAST (Kochukhov et al. 2010), InversLSD (Kochukhov et al. 2014), SoBAT (Anfinogentov et al. 2020), Corner (Foreman-Mackey 2016).

## ORCID iDs

Oleg Kochukhov  <https://orcid.org/0000-0003-3061-4591>  
Ansgar Reiners  <https://orcid.org/0000-0003-1242-5922>

## References

- Afram, N., & Berdyugina, S. V. 2019, *A&A*, **629**, A83  
Anfinogentov, S. A., Nakariakov, V. M., Pascoe, D. J., & Goddard, C. R. 2020, arXiv:2005.05365  
Astudillo-Defru, N., Delfosse, X., Bonfils, X., et al. 2017, *A&A*, **600**, A13  
Bagnulo, S., Landolfi, M., Landstreet, J. D., et al. 2009, *PASP*, **121**, 993  
Barklem, P. S., Piskunov, N., & O’Mara, B. J. 2000, *A&AS*, **142**, 467  
Bell, C. P. M., Mamajek, E. E., & Naylor, T. 2015, *MNRAS*, **454**, 593  
Bertaux, J. L., Lallement, R., Ferron, S., Boonne, C., & Bodichon, R. 2014, *A&A*, **564**, A46  
Boccaletti, A., Sezestre, E., Lagrange, A. M., et al. 2018, *A&A*, **614**, A52  
Boccaletti, A., Thalmann, C., Lagrange, A.-M., et al. 2015, *Natur*, **526**, 230  
Browning, M. K. 2008, *ApJ*, **676**, 1262  
Cohen, O., Drake, J. J., Gloer, A., et al. 2014, *ApJ*, **790**, 57  
Cook, B. A., Williams, P. K. G., & Berger, E. 2014, *ApJ*, **785**, 10  
Cranmer, S. R., Wilner, D. J., & MacGregor, M. A. 2013, *ApJ*, **772**, 149  
Dobler, W., Stix, M., & Brandenburg, A. 2006, *ApJ*, **638**, 336  
Donati, J.-F., Forveille, T., Cameron, A. C., et al. 2006, *Sci*, **311**, 633  
Donati, J.-F., Jardine, M. M., Gregory, S. G., et al. 2008a, *MNRAS*, **386**, 1234  
Donati, J.-F., Morin, J., Petit, P., et al. 2008b, *MNRAS*, **390**, 545  
Donati, J. F., Semel, M., Carter, B. D., Rees, D. E., & Collier Cameron, A. 1997, *MNRAS*, **291**, 658  
Donati, J.-F., Skelly, M. B., Bouvier, J., et al. 2010, *MNRAS*, **409**, 1347  
Fares, R., Donati, J.-F., Moutou, C., et al. 2010, *MNRAS*, **406**, 409  
Foreman-Mackey, D. 2016, *JOSS*, **1**, 24  
Gaia Collaboration, Brown, A. G. A., Vallenari, A., et al. 2018, *A&A*, **616**, A1  
Garraffo, C., Drake, J. J., & Cohen, O. 2016, *ApJL*, **833**, L4  
Grady, C. A., Wisniewski, J. P., Schneider, G., et al. 2020, *ApJL*, **889**, L21  
Greaves, J. S., Kennedy, G. M., Thureau, N., et al. 2014, *MNRAS*, **438**, L31  
Gustafsson, B., Edvardsson, B., Eriksson, K., et al. 2008, *A&A*, **486**, 951  
Hackman, T., Lehtinen, J., Rosén, L., Kochukhov, O., & Käpylä, M. J. 2016, *A&A*, **587**, A28  
Hawley, S. L., Davenport, J. R. A., Kowalski, A. F., et al. 2014, *ApJ*, **797**, 121  
Houdebine, E. R. 2010, *MNRAS*, **407**, 1657  
Houdebine, E. R., Mullan, D. J., Paletou, F., & Gebran, M. 2016, *ApJ*, **822**, 97  
Ibañez Bustos, R. V., Buccino, A. P., Flores, M., et al. 2019, *MNRAS*, **483**, 1159  
Johns-Krull, C. M. 2007, *ApJ*, **664**, 975  
Johns-Krull, C. M., & Valenti, J. A. 1996, *ApJL*, **459**, L95

- Johns-Krull, C. M., & Valenti, J. A. 2000, in ASP Conf. Ser. 198, *Stellar Clusters and Associations: Convection, Rotation, and Dynamos*, ed. R. Pallavicini, G. Micela, & S. Sciortino (San Francisco, CA: ASP), 371
- Johns-Krull, C. M., Valenti, J. A., & Koresko, C. 1999, *ApJ*, **516**, 900
- Kaeuffl, H.-U., Ballester, P., Biereichel, P., et al. 2004, *Proc. SPIE*, **5492**, 1218
- Kalas, P., Liu, M. C., & Matthews, B. C. 2004, *Sci*, **303**, 1990
- Kislyakova, K. G., Fossati, L., Johnstone, C. P., et al. 2018, *ApJ*, **858**, 105
- Kislyakova, K. G., Noack, L., Johnstone, C. P., et al. 2017, *NatAs*, **1**, 878
- Kochukhov, O. 2015, *A&A*, **580**, A39
- Kochukhov, O. 2016, in *Cartography of the Sun and the Stars*, Lecture Notes in Physics, Vol. 914, ed. J.-P. Rozelot & C. Neiner (Cham: Springer), 177
- Kochukhov, O., Heiter, U., Piskunov, N., et al. 2009, in AIP Conf. Proc. 1094, *Cool Stars, Stellar Systems and the Sun*, ed. E. Stempels (Melville, NY: AIP), 124
- Kochukhov, O., & Lavail, A. 2017, *ApJL*, **835**, L4
- Kochukhov, O., Lüftinger, T., Neiner, C., Alecian, E. & MiMeS Collaboration 2014, *A&A*, **565**, A83
- Kochukhov, O., Makaganiuk, V., & Piskunov, N. 2010, *A&A*, **524**, A5
- Kochukhov, O., Makaganiuk, V., Piskunov, N., et al. 2011, *ApJL*, **732**, L19
- Kochukhov, O., & Shulyak, D. 2019, *ApJ*, **873**, 69
- Landi Degl'Innocenti, E., & Landolfi, M. 2004, *Polarization in Spectral Lines*, Astrophysics and Space Science Library, Vol. 307 (Dordrecht: Kluwer Academic)
- Lang, P., Jardine, M., Morin, J., et al. 2014, *MNRAS*, **439**, 2122
- Lavail, A., Kochukhov, O., & Hussain, G. A. J. 2019, *A&A*, **630**, A99
- Lavail, A., Kochukhov, O., & Wade, G. A. 2018, *MNRAS*, **479**, 4836
- Lynch, B. J., Airapetian, V. S., DeVore, C. R., et al. 2019, *ApJ*, **880**, 97
- Makaganiuk, V., Kochukhov, O., Piskunov, N., et al. 2011a, *A&A*, **529**, A160
- Makaganiuk, V., Kochukhov, O., Piskunov, N., et al. 2011b, *A&A*, **525**, A97
- Mamajek, E. E., & Bell, C. P. M. 2014, *MNRAS*, **445**, 2169
- Manset, N., & Donati, J.-F. 2003, *Proc. SPIE*, **4843**, 425
- Martoli, E., Hebrard, G., Moutou, C., et al. 2020, *A&A*, **641**, L1
- Mathys, G. 1995, *A&A*, **293**, 733
- Mayor, M., Pepe, F., Queloz, D., et al. 2003, *Msngr*, **114**, 20
- Morin, J., Donati, J.-F., Petit, P., et al. 2008, *MNRAS*, **390**, 567
- Morin, J., Donati, J.-F., Petit, P., et al. 2010, *MNRAS*, **407**, 2269
- Newton, E. R., Irwin, J., Charbonneau, D., et al. 2016, *ApJ*, **821**, 93
- Newton, E. R., Irwin, J., Charbonneau, D., et al. 2017, *ApJ*, **834**, 85
- Petit, P., Louge, T., Théado, S., et al. 2014, *PASP*, **126**, 469
- Piskunov, N., Snik, F., Dolgoplov, A., et al. 2011, *Msngr*, **143**, 7
- Piskunov, N. E., & Valenti, J. A. 2002, *A&A*, **385**, 1095
- Plavchan, P., Barclay, T., Gagné, J., et al. 2020, *Natur*, **582**, 497
- Reiners, A., & Basri, G. 2006, *ApJ*, **644**, 497
- Reiners, A., & Basri, G. 2009, *A&A*, **496**, 787
- Rosén, L., Kochukhov, O., Hackman, T., & Lehtinen, J. 2016, *A&A*, **593**, A35
- Rosén, L., Kochukhov, O., & Wade, G. A. 2013, *MNRAS*, **436**, L10
- Ryabchikova, T., Piskunov, N., Kurucz, R. L., et al. 2015, *PhysS*, **90**, 054005
- Saar, S. H. 1994, in IAU Symp. 154, *Infrared Solar Physics*, ed. D. M. Rabin, J. T. Jefferies, & C. Lindsey (Dordrecht: Kluwer Academic), 493
- Saar, S. H., & Linsky, J. L. 1985, *ApJL*, **299**, L47
- Sharma, S. 2017, *ARA&A*, **55**, 213
- Shulyak, D., Reiners, A., Engeln, A., et al. 2017, *NatAs*, **1**, 0184
- Shulyak, D., Reiners, A., Nagel, E., et al. 2019, *A&A*, **626**, A86
- Shulyak, D., Reiners, A., Seemann, U., Kochukhov, O., & Piskunov, N. 2014, *A&A*, **563**, A35
- Snik, F., Kochukhov, O., Piskunov, N., et al. 2011, in ASP Conf. Ser. 437, *Solar Polarization 6*, ed. J. R. Kuhn et al. (San Francisco, CA: ASP), 237
- Strubbe, L. E., & Chiang, E. I. 2006, *ApJ*, **648**, 652
- Torres, C. A. O., Quast, G. R., da Silva, L., et al. 2006, *A&A*, **460**, 695
- Vidotto, A. A., Jardine, M., Morin, J., et al. 2013, *A&A*, **557**, A67
- Vidotto, A. A., Jardine, M., Opher, M., Donati, J. F., & Gombosi, T. I. 2011, *MNRAS*, **412**, 351
- Watson, C. A., Littlefair, S. P., Diamond, C., et al. 2011, *MNRAS*, **413**, L71
- Wende, S., Reiners, A., & Ludwig, H.-G. 2009, *A&A*, **508**, 1429
- White, R., Schaefer, G., Boyajian, T., et al. 2019, AAS Meeting, **233**, 259.41
- Wright, N. J., Newton, E. R., Williams, P. K. G., Drake, J. J., & Yadav, R. K. 2018, *MNRAS*, **479**, 2351
- Yadav, R. K., Christensen, U. R., Morin, J., et al. 2015, *ApJL*, **813**, L31
- Yang, H., & Johns-Krull, C. M. 2011, *ApJ*, **729**, 83
- Yang, H., Johns-Krull, C. M., & Valenti, J. A. 2008, *AJ*, **136**, 2286